



Accelerated simulations of direct shear tests by physics engine

Hantao He¹ · Junxing Zheng¹ · Zhaochao Li²

Received: 19 January 2020 / Revised: 9 June 2020 / Accepted: 14 June 2020
© OWZ 2020

Abstract

Physics engines, originally developed to simulate physical and mechanical processes in modern video games, are increasingly used as a scientific computational platform in many disciplines due to their high computational efficiency. This study explores the feasibility of using an open-source physics engine, Project Chrono, to simulate direct shear tests. This study develops a series of pre-processing, servo-controlling, and post-processing functions in Project Chrono to generate soil specimens with designed packing densities, perform direct shear tests, and output simulation results including stress-strain relations, fabrics, and force chains. To determine inter-particle contact forces, typical DEM codes use soft contact models, while most physics engines use hard contact models. The hard contact model enables physics engines to use large time steps in iterations without affecting the numerical stability and simulation accuracy, which remarkably reduces simulation time compared with typical DEM codes. Based on systematical comparisons between simulation results of two contact models, this study demonstrates that the hard contact model can yield the same direct shear test results observed in soft contact model simulations, but is ten times faster than the soft contact model for simulating the same number of particles. This study may provide DEM modelers with the physics engine as one more option for soil behavior simulation.

Keywords Direct shear test · Discrete element method · Physics engine · Soil behavior · Fabric

1 Introduction

The direct shear test is a simple laboratory test that divides the specimen into upper and lower parts and shears the specimen by pushing the lower part horizontally with a vertical load applied on top of the specimen. Direct shear tests are one of the most popular laboratory tests in geotechnical engineering to determine the strength parameters of soils.

Recently, numerical simulation methods, especially the discrete element method (DEM), have been developed rapidly and widely applied in modeling soil tests [1, 2]. Compared to actual laboratory tests, DEM can explicitly simulate

individual particles and their interactions, as well as obtain microscope particle behavior including particle velocity, particle rotation, and inter-particle contact force, which is intractable to measure in actual experiments [3].

The inter-particle contact model is the key to reproduce granular soil behavior. Typical DEM codes, such as Itasca PFC 2D/3D [4], LIGGGHTS [5], and YADE [6], use a soft contact model, originally proposed by Cundall [7–11]. Soft contact model allows overlap between contacting particles, and the amount of overlap determines the normal and frictional forces based on a force–displacement law. The key input contact parameters of the soft contact model include normal stiffness, shear stiffness, and friction coefficient. To yield small amounts of overlap compared to particle size, the normal and shear stiffnesses are usually set at very high values. Therefore, the time step size in the computation must be small to yield a small elastic rebound at each iteration to ensure numerical stability, which significantly increases simulation time when simulating a large number of particles.

In the area of computer science, simulations of rigid bodies and their interactions are important for video games and computer-animated films. Therefore, a physics-based simulation platform, physics engine, was developed to perform

✉ Junxing Zheng
juxing@iastate.edu

Hantao He
hhe@iastate.edu

Zhaochao Li
zli3@moreheadstate.edu

¹ Department of Civil, Construction, and Environmental Engineering, Iowa State University, Ames, IA 50011, USA

² Department of Engineering and Technology Management, Morehead State University, Morehead, KY 40351, USA

such simulations. For example, in Angry Birds game, collisions among birds, pigs, and blocks are simulated by a physics engine, called Box2D [12].

Physics engines primarily focus on simulation speed and stability to offer video game players an immersive and realistic gaming experience. Recently, with the rapid development of the computer gaming and movie industry, the accuracy, computational speed, and functionalities of physics engine techniques have been significantly improved, and have started to be used as a scientific computational platform in various disciplines, including geotechnical engineering [13], robotic control [14, 15], crowd simulation [16], biomedical engineering [17, 18], autonomous vehicle research [19], virtual and augmented reality [20], and psychological research [21].

Different from DEM codes, most physics engines use a hard contact model to compute contact forces. The hard contact model does not allow overlap between contacting particles. The velocities before collision are used to compute the velocities after collision. Then the Newton–Euler laws of motion are used to update the positions and orientations of the two particles and compute the contact force. The time step size used in the hard contact model can be large compared to the soft contact model without the risk of numerical instability. This reduces simulation times, especially when simulating many particles. Therefore, the physics engine provides a fast simulation speed so that players have real-time gaming experience [22, 23].

Effectiveness of DEM results depend on the number of particles used in the simulations. However, due to the limitations of available computational capability, the number of particles is usually reduced significantly at the cost of the effectiveness and accuracy of simulations [24]. The father of DEM, Cundall [24] optimistically predicted that the advance of computer hardware will enable DEM to simulate large-scale engineering problems and realistic soil and rock within 20 years. However, 20 years have passed. There is still a long way to go toward Cundall's wish. Therefore, if physics engines and hard contact model are proven effective and accurate for simulating granular soils, physics engines may be an excellent discrete element simulator due to their high computational efficiency.

The objective of this study is to evaluate the effectiveness and accuracy of physics engine techniques and hard contact models for simulating direct shear tests. A physics engine, called Project Chrono [25], is used in this study. Project Chrono is a physics-based modeling and simulation infrastructure implemented in C++, and it has been applied in multiple fields for performing scientific simulations, including robotics [26], vehicle dynamics [27], finite element analysis [28], and granular flows [29]. Project Chrono supports both soft and hard contact models, allowing comparisons of two contact models on the same platform. Therefore, it is

selected as the simulation platform. Specifically, this paper addresses the following two questions.

First, physics engines were initially developed for computer gaming. Therefore, these techniques do not provide pre-processing, servo-control, and post-processing functions for discrete element simulations. Therefore, this paper develops a series of functions that are embedded in Project Chrono, allowing Project Chrono to perform discrete element simulations of granular soils.

Second, this paper systematically compares theoretical formations, input parameters, numerical stability, computational speeds, and simulation results of hard and soft contact models for simulating direct shear tests. These comparisons help to evaluate the effectiveness and accuracy of hard contact model for simulating the shear behavior of granular materials.

We want to emphasize that the goal of this paper is *not* to use physics engines to replace any existing DEM codes such as PFC, LIGGGHTS, and Yade, or any other DEM codes. These existing codes are representing state-of-the-art platforms for DEM studies and applications. Our goal is to provide DEM modelers with physics engine as one more option that they may consider using when they are simulating granular materials.

2 Process flow of physics engine technique

The overall simulation flow is shown in Fig. 1. This study develops a series of functions embedded into Project Chrono allowing for performing direct shear simulations. The pre-processing functions are developed for creating specimens. Users can specify the size and the void ratio of specimens. The developed functions can automatically pack the particles to the target void ratio and size. Then, the specimen is input into the servo-control functions developed by this study to perform direct shear test simulations. Users can specify the shear speed, maximum shear displacement, and normal force.

The simulations are performed by the core computational functions in Project Chrono by a time-step procedure like DEM. First, it runs a collision detection program based on sweep and prune algorithm [30] to search the contacting particles. The details of sweep and prune algorithm can be found in He and Zheng [13] and Tracy et al. [30]. The contact forces between particles are computed based on contact models. Project Chrono includes both hard and soft contact models for users, which are compared in the next section. Then, linear and angular velocities of particles are updated based on contact forces based on Newton's second law. Finally, the positions and orientations of particles are updated based on Euler integration.

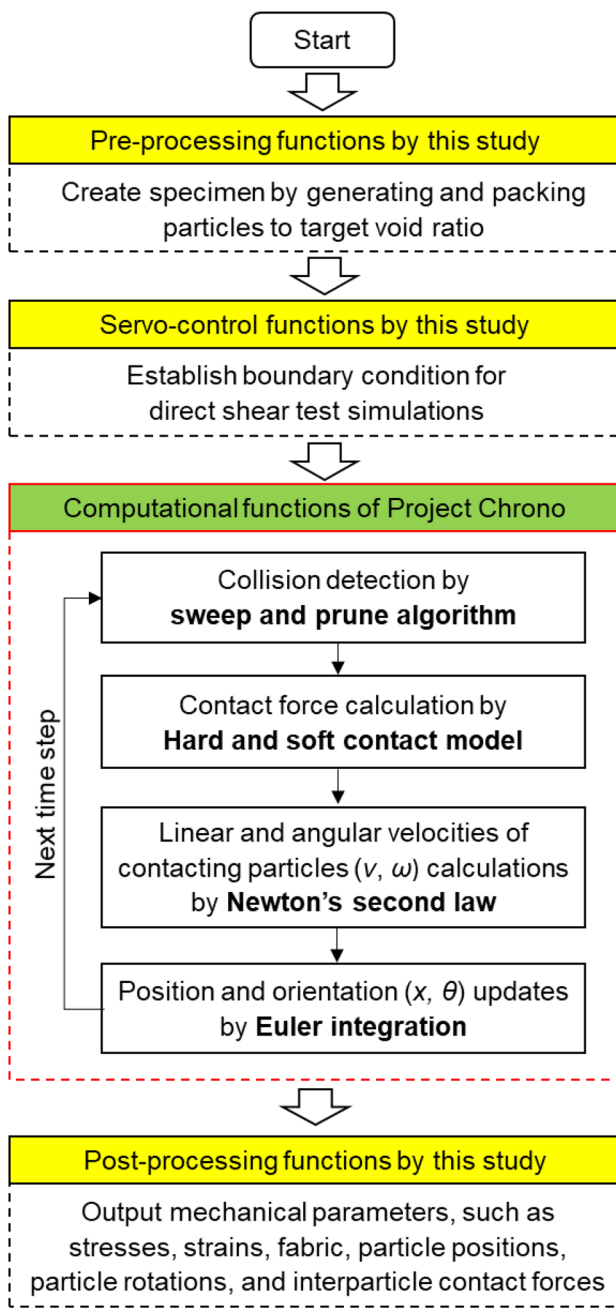


Fig. 1 Simulation flow of direct shear test using physics engine techniques

To output the mechanical parameters for analysis, post-processing and visualization functions are developed by this study. These functions are integrated into the computational functions in Project Chrono to store stress, strain, fabric, particle positions, particle rotations, and particle contact forces at each time step. Then, visualization functions are used to plot these mechanical parameters such as three-dimensional (3D) rose diagram of contact normals, 3D particle velocity fields, 3D particle rotation fields, and force chains.

2.1 Basic physics law of particle motion

Particle motions in both soft and hard contact models obey Newton's second law. Particle motions consist of linear and angular movements as shown in Fig. 2. Based on Newton's second law, linear and angular movements can be described as:

$$\mathbf{F} = m\mathbf{a} \quad (1)$$

$$\mathbf{M} = I\boldsymbol{\beta} \quad (2)$$

where \mathbf{F} , m , and \mathbf{a} are the force applied on the particle, the mass, and the linear acceleration of the particle; and \mathbf{M} , I , and $\boldsymbol{\beta}$ are the moment applied on the particle, the moment of inertia, and the angular acceleration of the particle, respectively.

The linear and angular velocities, as well as the displacement and rotation of particle, are computed iteratively. For example, in a semi-implicit Euler scheme, at time t , the linear and angular velocities can be computed as:

$$\mathbf{v}_{t+\Delta t} = \mathbf{v}_t + \mathbf{a}\Delta t = \mathbf{v}_t + \frac{\mathbf{F}_t\Delta t}{m} \quad (3)$$

$$\boldsymbol{\omega}_{t+\Delta t} = \boldsymbol{\omega}_t + \boldsymbol{\beta}\Delta t = \boldsymbol{\omega}_t + \frac{\mathbf{M}_t\Delta t}{I} \quad (4)$$

where Δt is the time step size used in the computation. Based on linear and angular velocities, the displacement and rotation of the particle at any time t can be computed as:

$$\mathbf{x}_{t+\Delta t} = \mathbf{x}_t + \mathbf{v}_{t+\Delta t}\Delta t \quad (5)$$

$$\boldsymbol{\theta}_{t+\Delta t} = \boldsymbol{\theta}_t + \boldsymbol{\omega}_{t+\Delta t}\Delta t \quad (6)$$

where \mathbf{x}_t and $\boldsymbol{\theta}_t$ are the displacement and rotation of the object at time t .

2.2 Formation of soft contact model

Many soft contact models have been developed as reviewed by Horabik and Molenda [31]. The basic concept of these soft contact models is essentially the same. The particle overlaps at contacts, and the magnitudes of contact forces are determined by the time-variant overlapping amount.

The soft contact model in Project Chrono is the Hertzian model, which has been widely used in DEM codes. The Hertzian model may be an analogy with a nonlinear spring-dashpot system. The spring represents the elastic contact force, and the dashpot governs the damping effect. For two particles in contact, the elastic force is positively correlated with the inter-particle overlap, and the damping force is determined by

Fig. 2 Illustration of particle movements following Newton's second law

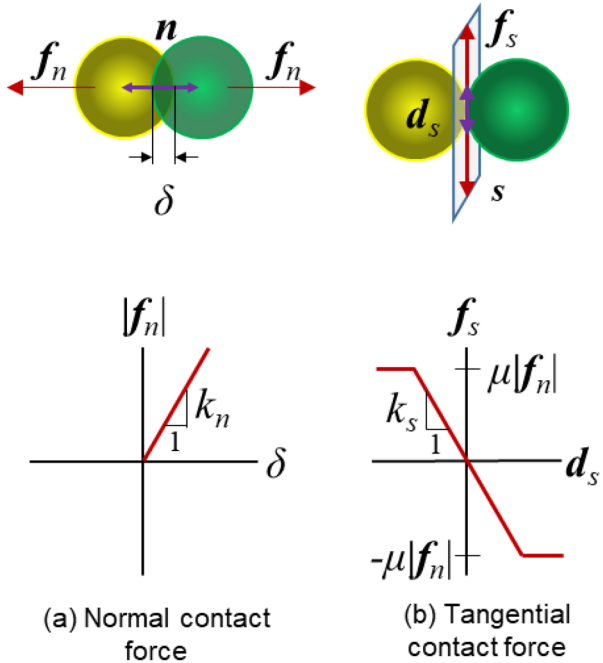
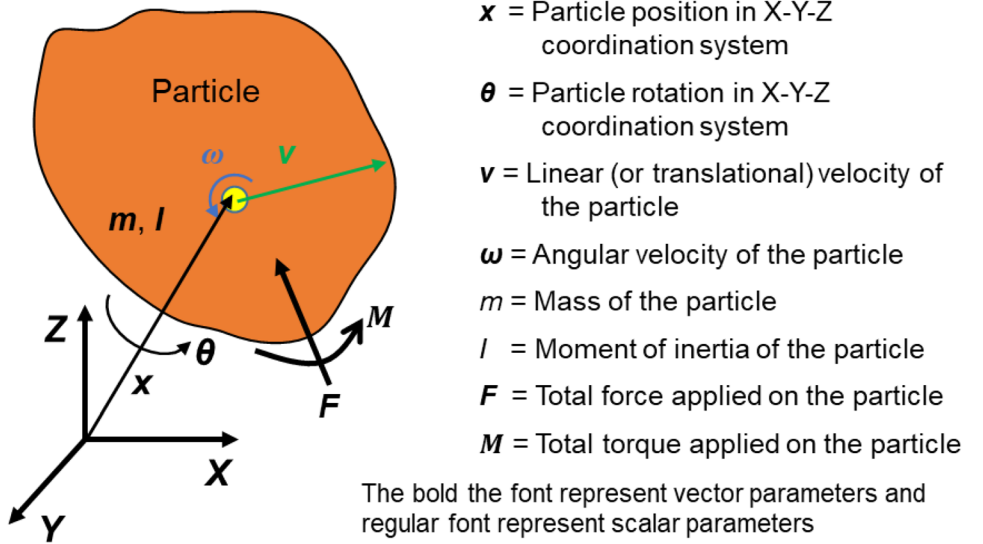


Fig. 3 The schematic of soft contact model

the damping ratio and the relative velocity. For example, two particles *i* and *j* are in contact in Fig. 3a, b, the inter-particle normal and tangential components of contact forces f_n and f_s can be determined as:

$$f_n = \sqrt{R_{\text{eff}}\delta}(k_n d_n - \gamma_n m_{\text{eff}} v_n) \quad (7)$$

$$f_s = \sqrt{R_{\text{eff}}\delta}(-k_s d_s - \gamma_s m_{\text{eff}} v_s) \quad (8)$$

where R_{eff} is the effective radius of curvature of two contacting particles; δ is the magnitude of overlap; k_n and k_s are the normal and tangential stiffness constants; d_n and d_s are the normal and tangential overlap vectors at the contact point; γ_n and γ_s are the normal and tangential damping coefficients; m_{eff} is the effective mass of two contacting particles; and v_n and v_s are the normal and tangential components of relative velocity at the contact point, respectively. Assuming the masses of two contacting particles are m_i and m_j , the effective mass m_{eff} and effective radius of curvature R_{eff} can be determined as:

$$m_{\text{eff}} = \frac{m_i m_j}{m_i + m_j} \quad (9)$$

$$R_{\text{eff}} = \frac{R_i R_j}{R_i + R_j}. \quad (10)$$

The relative velocity v and its normal and tangential components v_n and v_s can be computed as:

$$v = (v_j + \omega_j \times r_j) - (v_i + \omega_i \times r_i) \quad (11)$$

$$v_n = (v \cdot n)n \quad (12)$$

$$v_s = v - v_n \quad (13)$$

where v_i and v_j are the linear velocities of particles i and j ; ω_i and ω_j are the angular velocities of particles i and j ; \mathbf{r}_i and \mathbf{r}_j are the vectors pointing from the centers of masses of particles i and j to the contact point; and \mathbf{n} is the contact normal vector. Then, the normal and tangential overlapping vectors \mathbf{d}_n and \mathbf{d}_s can be determined as:

$$d_n = \delta n \quad (14)$$

$$d_s = \int_{t_0}^t v_s dt - \left(\mathbf{n} \cdot \int_{t_0}^t v_s dt \right) \mathbf{n} \quad (15)$$

where δ is the degree of overlap, t_0 is the time at the beginning of contact, and t is the current time.

The tangential contact force f_s can be determined using Coulomb's law of friction (stick-slip condition) as shown in Fig. 3b:

$$|f_s| = \begin{cases} |f_s| & \text{if } |f_s| < \mu |f_n| \\ \mu |f_n| & \text{if } |f_s| \geq \mu |f_n| \end{cases} \quad (16)$$

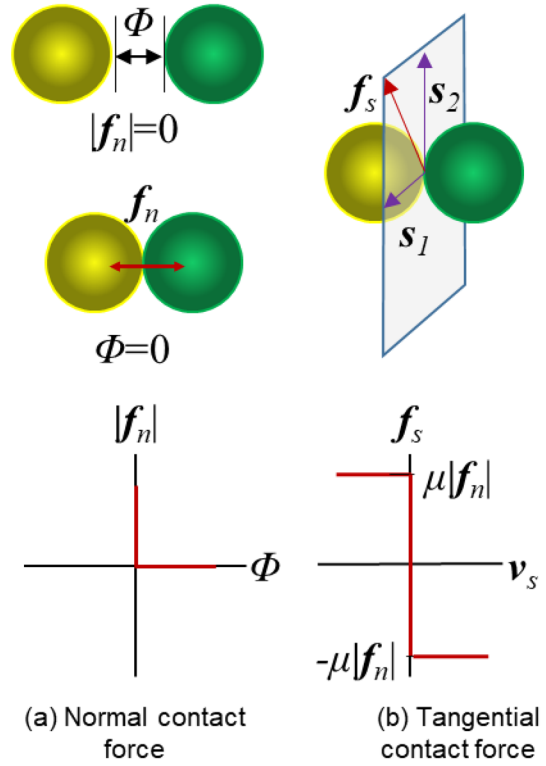
where μ is the friction coefficient. For low shear forces ($|f_s| < \mu |f_n|$), there is no relative motion between two particles (stick). For high shear forces ($|f_s| = \mu |f_n|$), there is relative motion between two particles (slip).

When simulating a particle assembly, the soft contact force of every contact point is computed separately and explicitly, with its own overlap distance and previous relative velocities. Thus, the soft contact model is easy to implement, and the computational cost for a single step is relatively low. However, the stiffness constants k_n and k_s must be set at high values and time step size Δt must be set at a small value in order to yield small amounts of overlapping compared to object size and to ensure computational stability and accuracy. This significantly increases computational time when simulating a large number of soil particles.

2.3 Formation of hard contact model

In the hard contact model, the contact forces are determined by satisfying two constraints: the normal component of contact force prevents the overlap between contacting objects, while the tangential component of contact force satisfies Coulomb friction law.

The Φ is the distance between two contacting particles i and j as shown in Fig. 4a. When $\Phi > 0$ (or particles i and j are separated), there is no normal contact force between particles i and j . When $\Phi = 0$ (or particles i and j are contacting), there might be a normal contact force f_n at the contact



Φ is the distance between two contacting particles
 f_n and f_s are normal and tangential contact forces
 μ is the interparticle friction coefficient
 v_s is tangential relative velocity of two particles

Fig. 4 The schematic of hard contact model

point for preventing the penetration. This is called Signorini unilateral contact condition.

Assuming s_1 and s_2 are two unit vectors perpendicular to each other on the shear plane as shown in Fig. 4b, the tangential contact force $f_s = f_{s1} + f_{s2}$ can be determined by the Coulomb friction law, which can be mathematically written as:

$$\sqrt{f_{s1}^2 + f_{s2}^2} \leq \mu |f_n| \quad (17)$$

$$(f_{s1} + f_{s2}) \cdot v_s = -\sqrt{f_{s1}^2 + f_{s2}^2} |v_s| \quad (18)$$

$$|v_s| \left(\mu |f_n| - \sqrt{f_{s1}^2 + f_{s2}^2} \right) = 0. \quad (19)$$

Equation (17) shows the upper limit of the magnitude of f_s in Coulomb friction law. Equation (18) means that f_s and v_s are collinear in the opposite direction. Equation (19) shows that the stick-slip condition: if $|v_s| > 0$, a relative sliding motion occurs between two contacting particles and

$\left(\mu|f_n| - \sqrt{f_{s1}^2 + f_{s2}^2}\right) = 0$; if $|v_s| = 0$, no sliding motion occurs between two contacting particles $\left(\mu|f_n| - \sqrt{f_{s1}^2 + f_{s2}^2}\right) \geq 0$. This can be also mathematically written as:

$$|v_s| \geq 0,$$

$$\left(\mu|f_n| - \sqrt{f_{s1}^2 + f_{s2}^2}\right) \geq 0, \quad |v_s| \left(\mu|f_n| - \sqrt{f_{s1}^2 + f_{s2}^2}\right) = 0. \quad (20)$$

In this case, the set of possible friction forces is two-dimensional resulting in a mathematically complicated problem. Then, the maximum dissipation principle is applied to solve such a complication problem [32]. According to the maximum dissipation principle, with the normal contact force f_n , the friction force f_s is the one that maximizes the rate of energy dissipation $|v_s| \cdot |f_s|$. Since f_s and v_s are collinear in the opposite direction, the maximum dissipation principle minimizes $v_s \cdot f_s$. Thus, the calculation of f_{s1} and f_{s2} becomes an optimization problem as:

$$(|f_{s1}|, |f_{s2}|) = \arg \min_{\sqrt{x^2+y^2} \leq \mu|f_n|} v_s(xs_1 + ys_2). \quad (21)$$

When simulating a particle assembly, hard contact forces at all the contact points are computed simultaneously using Eqs. (17)–(21) to satisfy the equilibrium of the particle system, forming a nonlinear complementarity problem. Nowadays, there are various types of solvers to solve complementarity problems, for example, Project Chrono uses a differential variational inequality (DVI) method to solve such problems [32]. Unlike the soft contact model, the hard contact model needs contact forces of all contact points to be solved simultaneously. Therefore, the computational cost for a single step in hard contact simulations is higher than the computational cost in soft contact simulations. Also, the problem is nonlinear, so it has to be solved implicitly, making the implementation more difficult than the soft contact model. However, the time step size used in the hard contact model can be large compared to the soft contact model without the risk of numerical instability. Therefore, less iterations are required for conducting a simulation, which reduces simulation time, especially when simulating a large number of particles.

3 Direct shear test simulations

In this paper, direct shear tests were simulated in Project Chrono with both soft and hard contact models. A total of 10,000 spheres with a radius of 2.5 mm were used in the simulation. The specimens were prepared at dense and loose conditions by setting the inter-particle friction coefficient

μ of spheres as 0 (dense) and 1 (loose) initially. Then, the spheres rain fell into the direct shear box with a cross section of 10 cm \times 10 cm and the top plate was added on the top of the specimen. The specimens were consolidated under the normal stress of 100 kPa. After the system reached its stable state, the heights of dense and loose specimens were 10.3 cm and 11.7 cm, respectively. The void ratios of dense and loose specimens were 0.58 and 0.73, respectively. Figure 5a shows the dense specimen after consolidation. The actual direct shear specimen typically has a dimension of 10 cm \times 10 cm \times 6 cm. In this research, we designed a cubic direct shear specimen. The purpose is to minimize the

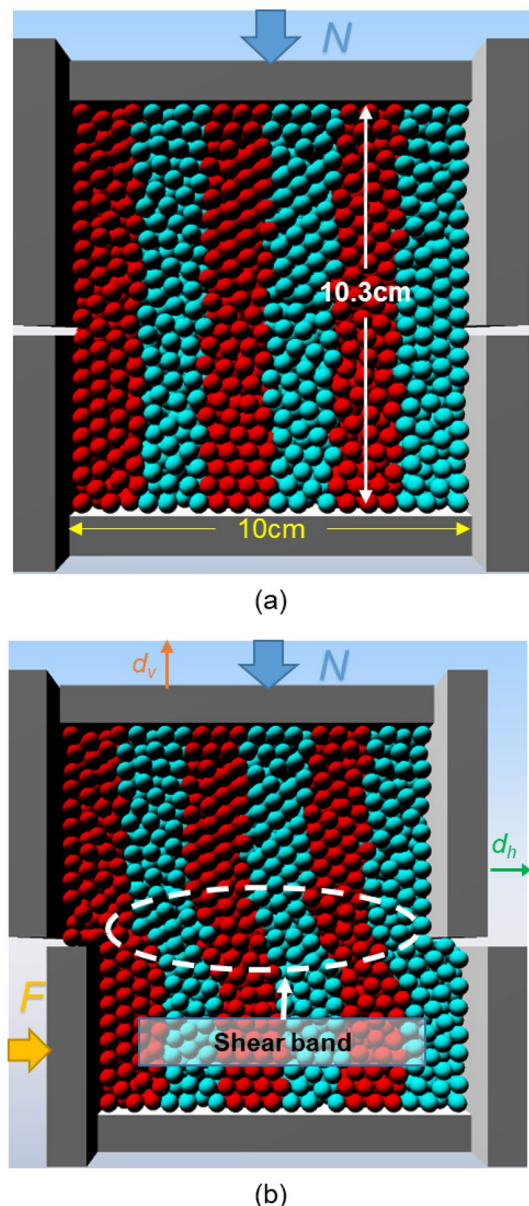


Fig. 5 The direct shear simulation setups for a dense specimen: **a** after consolidation; **b** after shear

boundary effects on shear band formation and development as shown in Fig. 5b.

In the shear stage, the friction coefficient μ of spheres was set as 0.1. Based on Cui and O'Sullivan [33] and O'Sullivan et al. [34], the μ of chrome steel balls was approximately 0.1. Therefore, this value was also used in this study. We also used $\mu=0.2$ and 0.3 to investigate the relationships between μ and shear strength. Then, the specimens were sheared using a speed of 0.024 mm/min following ASTM D3080 [35] until the horizontal displacement reached 10 mm as shown in Fig. 5b. Both soft and hard contact models were used in simulations and simulation parameters are shown in Table 1. The simulations are performed on a desktop with

Table 1 Simulation parameters of soft and hard contact models

Parameters	Soft contact model	Hard contact model
Ball density (kg/m ³)	7850	
Friction coefficient, μ	0.1 (dense and loose); 0.2, 0.3 (only dense)	
Young's modulus, E (Pa)	4×10^9	—
Poisson's ratio	0.27	—
Normal contact stiffness, k_n (N/m)	10^{12}	—
Tangential contact stiffness, k_t (N/m)	8×10^{11}	—
Normal damping coefficient, γ_n (s ⁻¹)	40	—
Tangential damping coefficient, γ_t (s ⁻¹)	20	—
Restitution coefficient	—	0.87
Time step size, Δt (s)	10^{-5}	10^{-3}

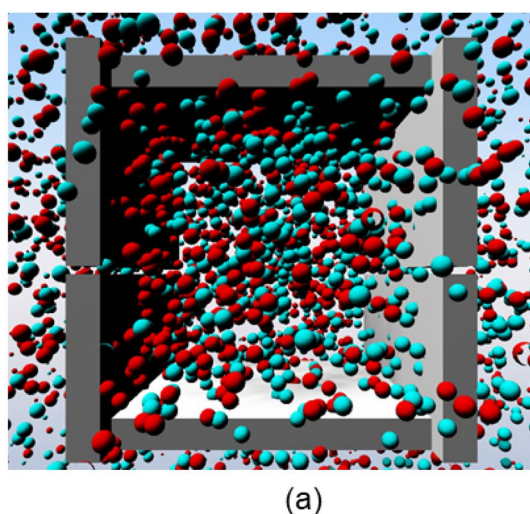
an Intel Xeon E5-1620 3.6 GHz 8-Core CPU, 16 GB memory, and a NVIDIA Quadro K620 GPU with 2 GB graphic memory.

4 Simulation result analysis

4.1 Time step size and simulation speeds

Time step size (Δt) is critical for yielding valid simulation results. A large time step size can expedite the simulation but may affect the simulation accuracy and stability. In both soft and hard contact models, an excessively large time step may cause penetration between contacting particles or erroneously large post-collision velocities, resulting in explosive effects as shown in Fig. 6a. The simulated explosive effects in Fig. 6a are based on soft contact model. The hard contact model results in the same effects using large time step, so it is not shown. This section evaluates the maximum allowable time step size (Δt_{\max}) as a function of particle stiffnesses (E).

To determine Δt_{\max} , we enlarge the time step by 10 times and run the simulation each time, until the explosive effect occurs in the simulation. Then, the largest time step size which still keeps the simulation stable is defined as Δt_{\max} . To investigate the effects of E values on Δt_{\max} in the soft contact model, the Δt_{\max} values for different E values were determined as shown in Fig. 6b. Expectedly, larger E values result in smaller Δt_{\max} values in the soft contact model. However, in the hard contact model, Δt_{\max} does not depend on particle stiffness because particles are perfectly rigid or E is infinite large, so the Δt_{\max} can be set as a large value regardless of particle stiffness as shown in Fig. 6b.



(a)

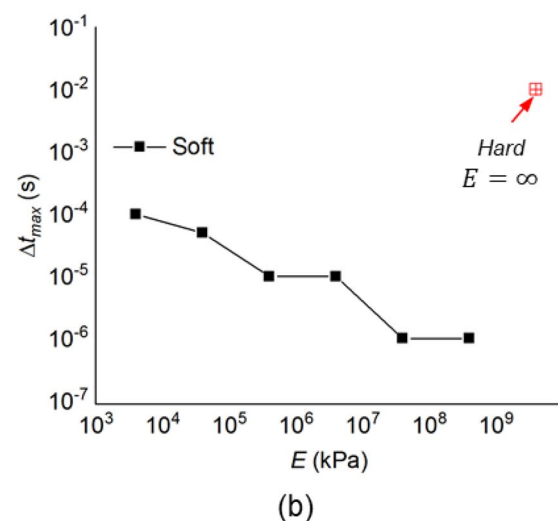


Fig. 6 The maximum allowable time step size in simulations: **a** explosive effect of particle assembly when using an excessively large time step and soft contact model; **b** the maximum allowable time step sizes for hard and soft contact models

The computational load and time increase as the increasing number of particles in the specimen. The numbers of spheres in the soil specimen were set as 100, 500, 1000, 5000, 10,000, and the sizes of spheres were adjusted to maintain approximately the same dimensions of specimens (10 cm in length \times 10 cm in width \times 10 cm in height). Simulations were repeated using both soft and hard contact models, and their time costs were compared. The $\Delta t = 10^{-3}$ s was used in the hard contact model, and $\Delta t = 10^{-5}$ s was used in the soft contact model.

The computational time for a single iteration step using the different numbers of spheres is shown in Fig. 7a. For completing one iteration step, the computational time in the soft contact model is faster than the computational time in the hard contact model by about one order of magnitude. However, the time step in the soft contact model must be small. Therefore, more time steps are required for completing the simulation. The time step in the hard contact model can be large and less time steps are required for completing the simulation. Therefore, it is observed that the total computational time for the hard contact model is approximately ten times shorter than the soft contact model in Fig. 7b.

4.2 Stress-strain behavior

The global shear strain ϵ_s is defined as:

$$\epsilon_s = \frac{d_h}{L} \quad (22)$$

where d_h is horizontal displacement of shear box, and L is the length of shear box.

The relationship between the ratio of shear force F to normal force N (F/N) versus global shear strain ϵ_s is shown in Fig. 8a, b. The relationship between vertical displacement

(d_v) and ϵ_s is shown in Fig. 8c, d. Both hard and soft contact models capture contraction and dilation behavior of loose and dense granular soils under shear. They both yield the same residual strength.

The mobilized friction angle ϕ can be calculated as:

$$\phi = \arctan \left(\frac{F}{N} \right). \quad (23)$$

The peak friction angles (ϕ_p) of hard and soft contact models are compared in Table 2. The agreement is remarkable. The maximum divergence is within 2° .

The dilation angle ψ can be calculated as:

$$\psi = \arctan \left(\frac{\Delta d_v}{\Delta d_h} \right). \quad (24)$$

Relationships between ψ and ϵ_s are shown in Fig. 8e, f. The peak dilation angles (ψ_p) of all the simulations agree well in Table 2. The maximum divergence is within 2° .

4.3 Particle motion

4.3.1 Particle displacement

The displacement fields of all the particles at both dense and loose specimens using both hard and soft contact models are shown in Fig. 9. Each arrow represents the displacement vector of a particle. The color as well as the length of bar represents the magnitude of the displacement. In both loose and dense simulations, particles in the lower half of the direct shear box move right along with the direct shear box. In the upper half of the shear box, most particles moved downwards in loose specimens (contraction) and upwards in dense specimens (dilation). The displacement fields are visually the same between hard and software contact models.

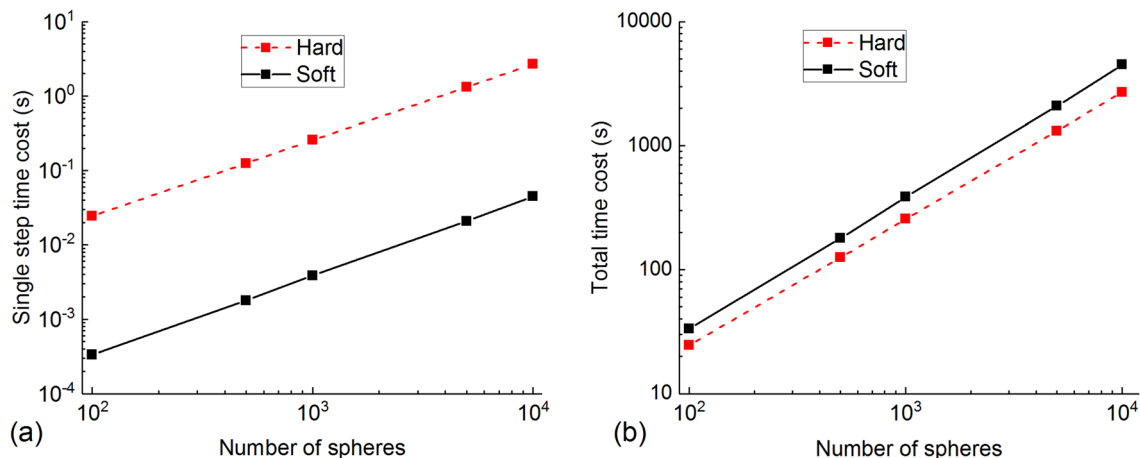


Fig. 7 Comparisons of single step time cost and total time cost between hard and soft contact models

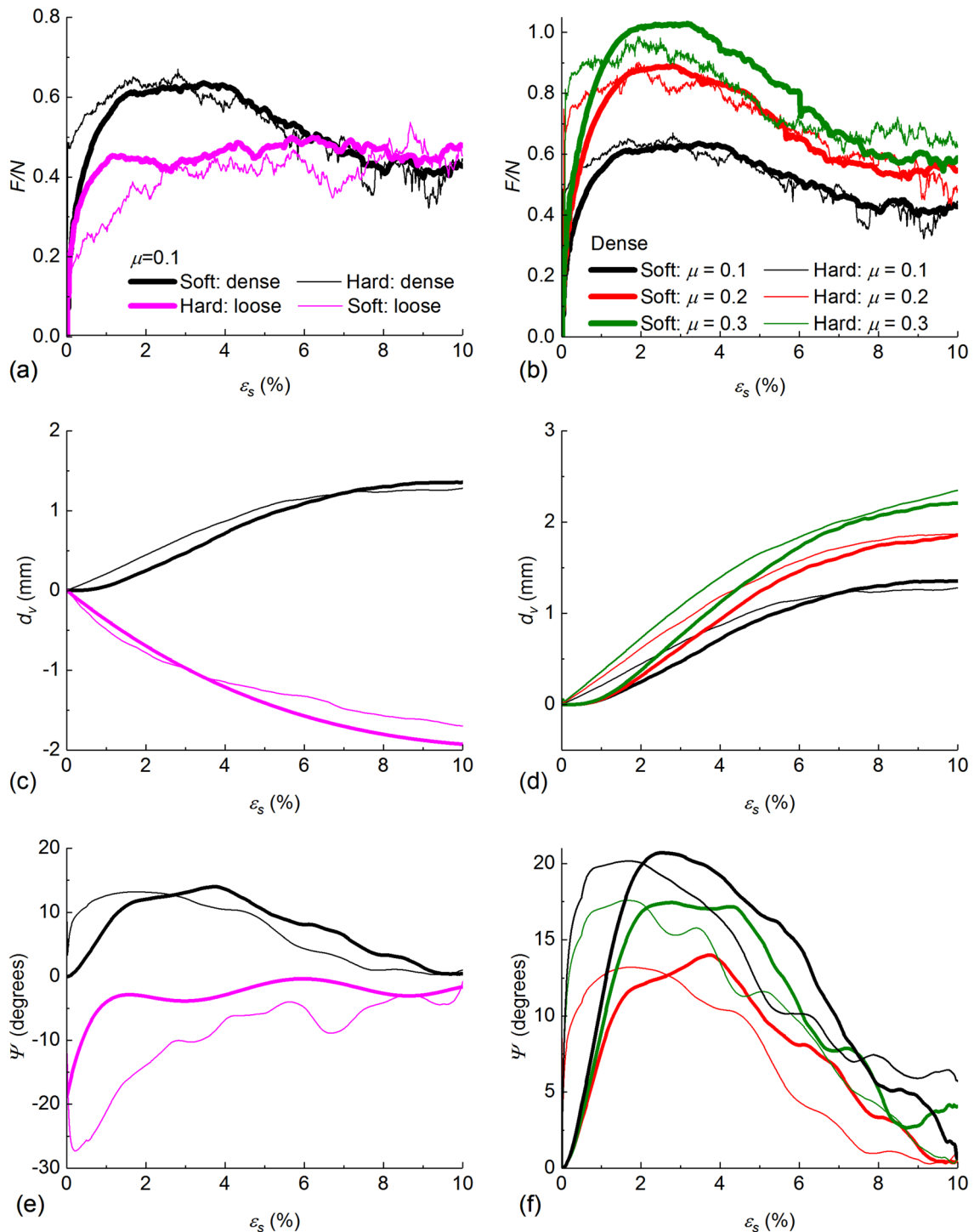


Fig. 8 Simulated stress–strain behavior using hard and soft contact models: **a, c, e** evolutions of force ratios, vertical displacements, and dilation angles for loose and dense specimens at $\mu=0.1$; **b, d, f** evolu-

tions of force ratios, vertical displacements, and dilation angles different μ values at dense condition

Particle horizontal displacements as a function of particle vertical position are shown in Fig. 10. The vertical position of the upper surface of the lower half direct shear box is considered as zero in the vertical axis. In both loose and dense

conditions, the horizontal displacements of particles in the upper and lower zones are tightly strained, while the displacements in the middle shear zone distribute among the entire horizontal axis. The middle shear zones can be considered as

Table 2 Comparisons of peak friction angles and dilation angles between hard and soft contact models

Parameters	Hard contact model	Soft contact model
ϕ_p (°)		
Loose		
$\mu=0.096$	28.2	26.5
Dense		
$\mu=0.096$	33.9	32.4
$\mu=0.2$	42.0	41.7
$\mu=0.3$	44.6	45.8
ψ_p (°)		
Loose		
$\mu=0.096$	-0.1	-0.4
Dense		
$\mu=0.096$	13.2	14.0
$\mu=0.2$	17.5	17.4
$\mu=0.3$	20.2	20.7

shear bands. Both soft and hard contact models yield the same shear band between -2 and 2 cm in the vertical direction.

4.3.2 Instant velocity

The instant velocities of both dense and loose specimens when $\varepsilon_s=5\%$ in both soft and hard contact models are shown in Fig. 11. Each arrow represents the velocity vector of a particle. The direction of the bar represents the direction of the velocity, and the color represents the magnitude of the velocity, or the speed. In both soft and hard contact models, in the upper half of the shear box, the velocities of most particles point upwards in dense specimens and downwards in loose specimens. In addition, the speeds are larger in the lower half direct shear box than in the upper box in all cases. The instant velocities of particles computed by both hard and soft contact models are visually the same as shown in Fig. 11.

4.4 Particle rotation

The particle rotations can be quantified in the form of quaternion. Assuming an object has a rotation θ about a rotation axis $\mathbf{u}=[u_x, u_y, u_z]$, where u_x, u_y, u_z are the components of \mathbf{u} along x, y , and z axes as shown in Fig. 12, a quaternion \mathbf{Q} can be defined to represent the rotation of a particle:

$$\mathbf{Q} = \begin{bmatrix} q_0 \\ q_1 \\ q_2 \\ q_3 \end{bmatrix} = \begin{bmatrix} \cos\left(\frac{\theta}{2}\right) \\ u_x \sin\left(\frac{\theta}{2}\right) \\ u_y \sin\left(\frac{\theta}{2}\right) \\ u_z \sin\left(\frac{\theta}{2}\right) \end{bmatrix}. \quad (25)$$

Thus, with quaternion \mathbf{Q} obtained by simulations, rotation θ can be calculated as:

$$\theta = 2 \arccos(q_0). \quad (26)$$

Particle rotations in the dense specimen using soft and hard contact models are shown in Fig. 13a, b. Particle rotations in the loose specimen using both contact models are shown in Fig. 13c, d. Most particles with larger rotations highly concentrate in the middle of the shear box (shear band), due to significant colliding and rubbing in this region. The previously identified shear band (-2 cm and 2 cm) in Fig. 10 is also superimposed in Fig. 13. As shown, the majority of particle rotation occurs within the shear band.

Figure 14a, b shows the average rotation (θ_{mean}) values of all the particles, as well as of the particles in the shear bands in dense and loose specimens, respectively. In both dense and loose specimens, the θ_{mean} of the hard contact model is approximately twice larger than the θ_{mean} of the soft contact model. In addition, both hard and soft contact models demonstrate that the θ_{mean} of particles in the shear band is approximately twice larger than the θ_{mean} of all the particles.

4.5 Fabric analysis

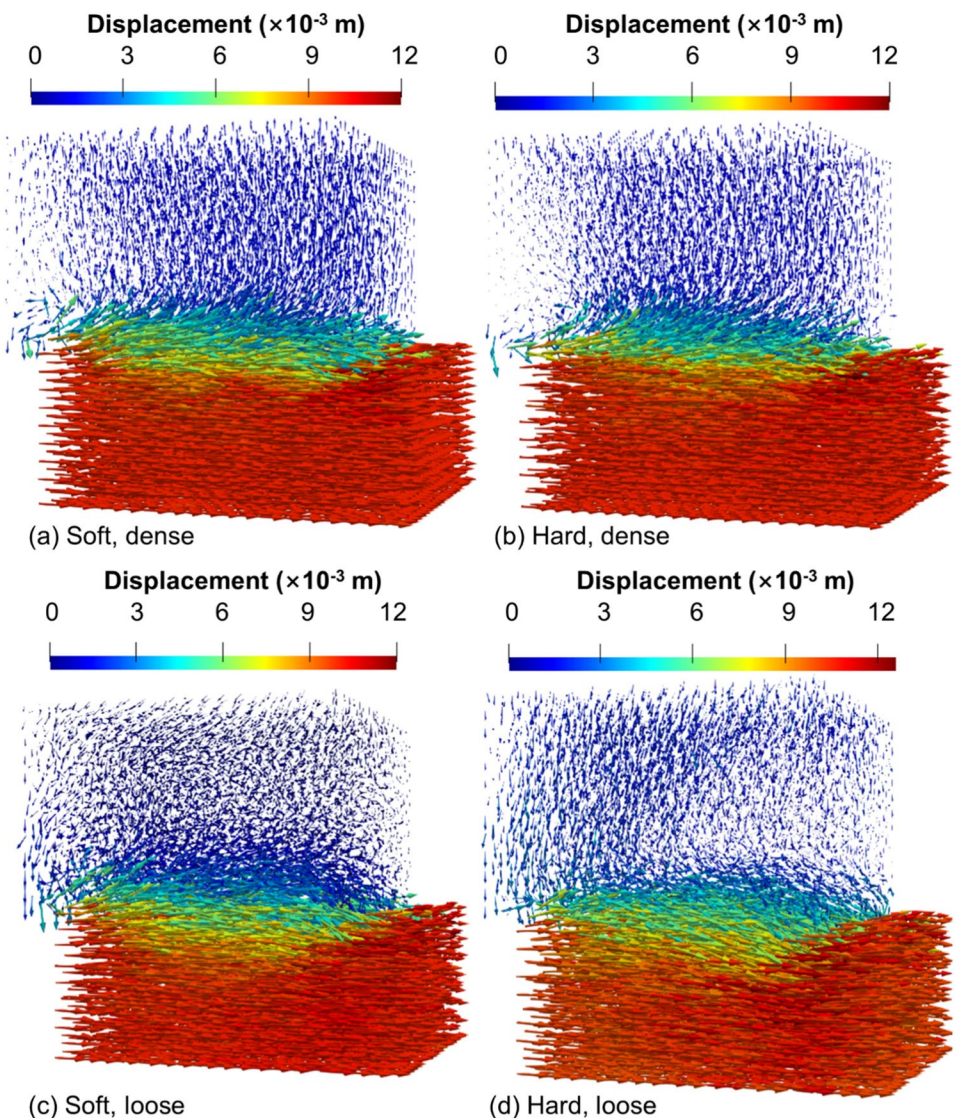
Soil specimen fabric can be quantified by scalar parameters (such as coordination number, contact index, the average branch vector length, etc.) and directional parameters (such as spatial distributions of particle long axes, contact normals, branch vectors, etc.) [36, 37]. The coordination number and spatial distribution of contact normals are widely used for analyzing fabric evolution in DEM simulations, and therefore these parameters in both contact models are obtained and compared in this study.

4.5.1 Coordination number

The coordination number (CN) is quantified as the average number of contacts of a single particle in a granular system. Larger CN means stronger fabric formed in granular soils. If the total number of particles is N_p in the soil specimen and the total number of contacts is N_c , the CN is defined as:

$$CN = \frac{2N_c}{N_p}. \quad (27)$$

Fig. 9 Particle displacement vectors using soft and hard contact models with $\mu=0.1$ at $\epsilon_s=10\%$



The CNs of all the particles at loose and dense specimens using hard and soft contact models with $\mu=0.1$ are shown in Fig. 15a. The CNs of the particles in the shear band identified in Fig. 10 are shown in Fig. 15b. In dense specimens, CN values decrease with the shearing process in both contact models. In loose specimens, CN values increase with the shearing process. This is because dense soil specimens dilate when they are sheared, while loose soil specimens become denser during the shearing process.

The CNs of dense specimens with $\mu=0.1, 0.2$ and 0.3 are plotted in Fig. 15c and the CNs of the particles in the shear band are shown in Fig. 15d. Larger μ leads to low CN no matter what contact model is used. This is because larger μ causes larger dilation, looser specimen, and therefore, smaller CN.

The same trends of CNs are captured by both soft and hard contact models for all the particles or only the

particles in the shear band. However, the hard contact model yields larger CN values than the soft contact model. Therefore, more contacts are generated in simulations using the hard contact model.

4.5.2 Contact normal

Contact normals are vectors representing the normal directions of contact forces on contact points in a soil specimen. The spatial distribution of contact normals can be plotted as a 3D rose diagram as shown in Fig. 16c–j. Each bar represents the frequency of contact normals in this direction in the 3D space.

Kanatani [38] showed that the rose diagram can be quantified by a density function $f(n)$:

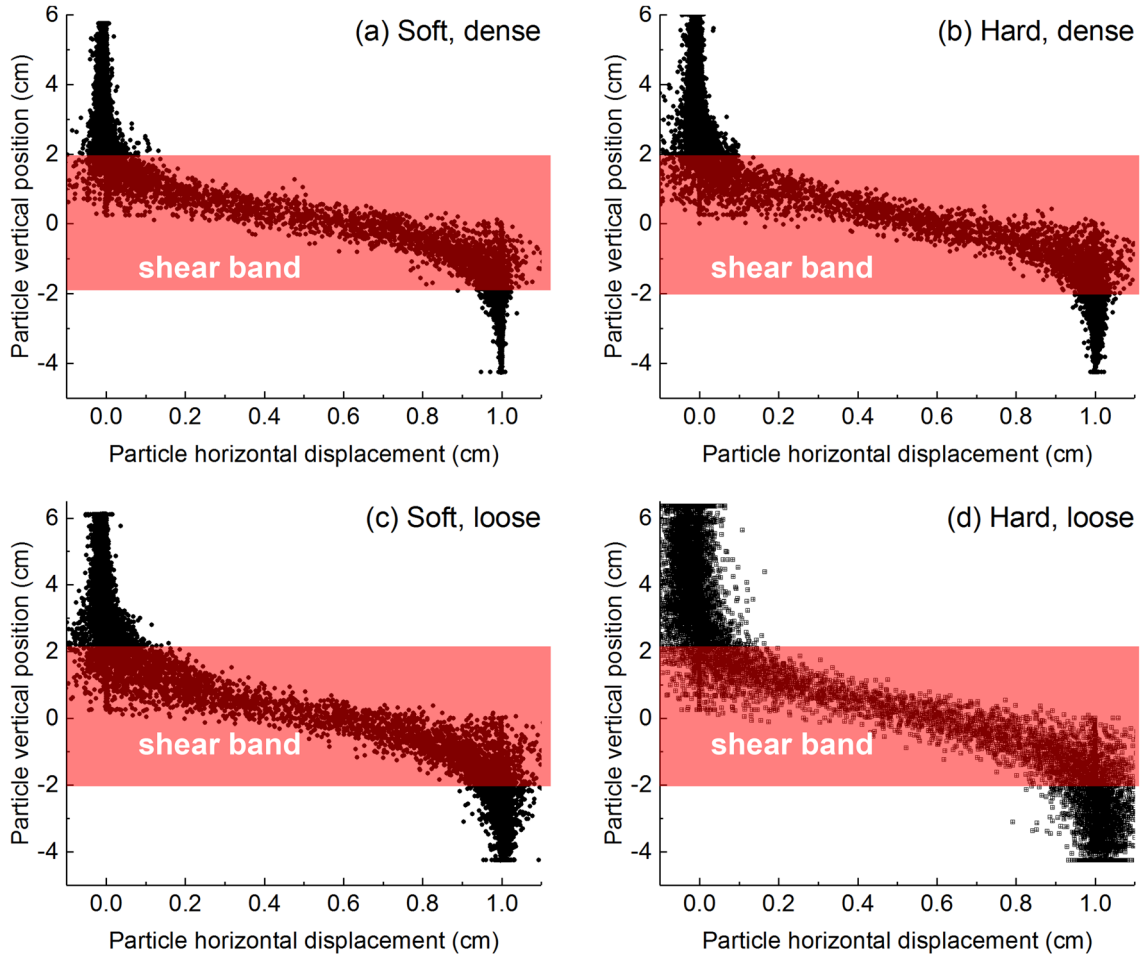


Fig. 10 Particle horizontal displacement versus vertical position using soft and hard contact models with $\mu=0.1$ at $\varepsilon_s=10\%$

$$f(n) = \frac{1}{2\pi} (1 + D_{ij}n_i n_j + D_{ijkl}n_i n_j n_k n_l) \quad (i, j = 1, 2, 3) \quad (28)$$

where n_i is the component of contact normal in axis i , and D_{ij} and D_{ijkl} are the second order deviatoric tensor, and the fourth order deviatoric tensors, respectively:

$$D_{ij} = \frac{2}{15} \left(\varphi_{ij} - \frac{1}{3} \delta_{ij} \right) \quad (29)$$

$$D_{ijkl} = \frac{2}{15} \left(\varphi_{ijkl} - \frac{6}{7} \delta_{ij} \varphi_{kl} + \frac{3}{35} \delta_{ij} \delta_{kl} \right) \quad (30)$$

where δ_{ij} is the Kronecker delta function:

$$\delta_{ij} = \begin{cases} 1 & i=j \\ 0 & i \neq j \end{cases} \quad (31)$$

and φ_{ij} and φ_{ijkl} are second order and fourth order fabric tensors, respectively:

$$\varphi_{ij} = \frac{1}{N_c} \sum_{m=1}^{N_c} n_i^m n_j^m \quad (32)$$

$$\varphi_{ijkl} = \frac{1}{N_c} \sum_{m=1}^{N_c} n_i^m n_j^m n_k^m n_l^m \quad (33)$$

where N_c is the total number of contact normals in the soil.

The contact normals for plotting the rose diagram are also used to determine density function based on Eqs. (28)–(33), which is also plotted in Fig. 16c–j. The density function is essentially the best fitting surface of the 3D rose diagrams. Both 3D rose diagram and density function illustrate the preferred direction of contact normals, but 3D rose diagram may be easier for visual observation of the preferred direction.

Figure 16c–f plots 3D rose diagrams and density functions for all the contact normals. After the consolidation

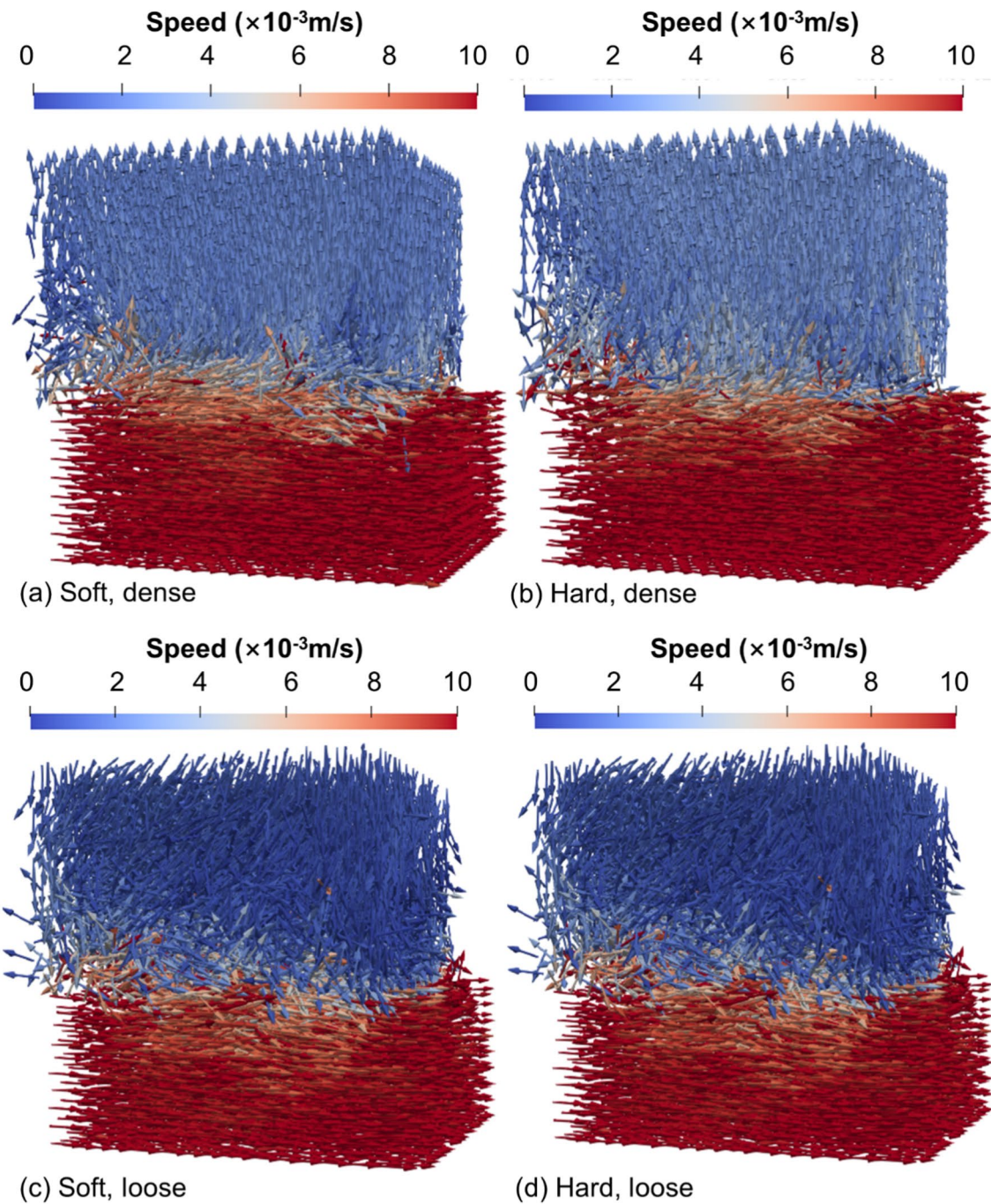


Fig. 11 Instant velocity vectors using soft and hard contact models with $\mu=0.1$ at $\varepsilon_s=10\%$

as shown in Fig. 14a, the isotropic fabric is observed due to confining and normal stresses from the direct shear box as shown in Fig. 16c, e. After the shear stage as shown in Fig. 16b, the resistant force along the diagonal direction of the specimen mobilizes more contact normals in this direction. Therefore, the 3D rose diagrams are skewed diagonally, exhibiting an anisotropic fabric as shown in Fig. 16d, f. Both hard and soft contact models determine

similar rose diagrams and densities functions for all the contact normals.

Figure 16g–j plots 3D rose diagrams and density functions for contact normals in the shear band. After consolidation, the preferred vertical direction is observed as shown in Fig. 16g, i. After shear, the stronger preferred diagonal direction is observed for contact normals in the shear band as shown in Fig. 16i, j. Both hard and soft contact models

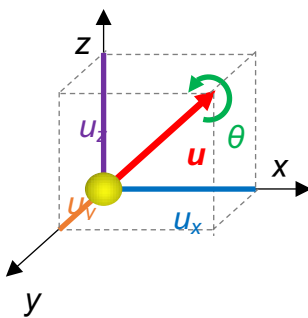


Fig. 12 Illustration of particle rotation

determine similar rose diagrams and densities functions for the contact normals in the shear band.

The second-order fabric tensor φ_{ij} is a 3-by-3 matrix. Three principal values (eigenvalues) of the fabric tensor are φ_1 , φ_2 , and φ_3 , which are commonly used for advanced geotechnical analysis, such as development anisotropic constitutive models and quantification of fabric anisotropy [39–43]. To measure the degree of fabric anisotropy, Barreto and O'Sullivan [44] proposed a generalized octahedral fabric factor based on φ_1 , φ_2 , and φ_3 values:

$$\Psi = \frac{1}{\sqrt{2}} \left[(\varphi_1 - \varphi_2)^2 + (\varphi_1 - \varphi_3)^2 + (\varphi_2 - \varphi_3)^2 \right]^{0.5}. \quad (34)$$

The evolutions of Ψ of contact normals in dense and loose specimens using hard and soft contact models with $\mu=0.1$ are shown in Fig. 17a. The evolutions of Ψ of contact normals in the shear band identified in Fig. 10 are shown in Fig. 17b. Larger Ψ values and therefore stronger fabric anisotropy are observed for contact normals in shear bands.

The evolutions of Ψ of contact normals in dense specimens with $\mu=0.1$, 0.2 and 0.3 are plotted in Fig. 17c and evolutions of Ψ of contact normals in the shear band are shown in Fig. 17d. Larger μ leads to larger Ψ values and stronger fabric anisotropy.

Similar trends of Ψ are captured by both soft and hard contact models for all the particles or only the particles in the shear band. However, the soft contact model yields larger Ψ values and therefore stronger fabric anisotropy than the hard contact model.

4.6 Force chains

Force chains are a key feature of DEM for visualizing the heterogeneity of granular systems under external loads.

Force chains allowed DEM researchers to directly observe micro inter-particle force transmission and link micro- and macro-mechanical behavior of granular soils. This study developed functions that can be embedded into Project Chrono to plot force chains. Figure 18 shows the chain forces in both contact models with different shear strains. Each bar represents an inter-particle contact force. The color and size of the bar represent the magnitude of the force, and the direction of the bar represents the direction of the contact force.

After consolidation ($\epsilon_s=0$) in Fig. 18a, b, the directions of inter-particle contact forces are randomly distributed for both contact models. The magnitudes of contact forces are approximately the same. After the shearing stage ($\epsilon_s=10\%$) in Fig. 18c, d, more inter-particle contact forces in diagonal direction are mobilized. According to Fig. 18, the hard contact model can generate similar force chains as the soft contact model.

5 Conclusion

Physics engine techniques utilize a hard contact model, which can accelerate DEM simulations compared with the soft contact model which is typically used in DEM codes. To address the limitations of physics engine that lack pre-processing, servo-controlling, and post-processing functions for DEM simulations, this paper developed a series of functions that can be embedded into Project Chrono, allowing Project Chrono to perform direct shear simulations. Then, this study compared the formations and simulation results of hard and soft contact models based on the improved Project Chrono platform.

This study showed that when simulating the same number of spheres, the speed of the hard contact model is approximately ten times faster than the speed of the soft contact model. The direct shear simulation results demonstrated that the hard contact model successfully captured key parameters of the macro shear behavior of granular soils including peak and residual shear strength, and maximum dilatancy. Hard and soft contact models generated the same microparticle-level behavior under shear such as the displacement field, speed, shear band, and particle rotations.

The similar trends of fabric simulations were observed for hard and soft contact models. However, the hard contact model yielded larger CNs and smaller Ψ than the soft contact model. Both contact models computed the visually same force chains.

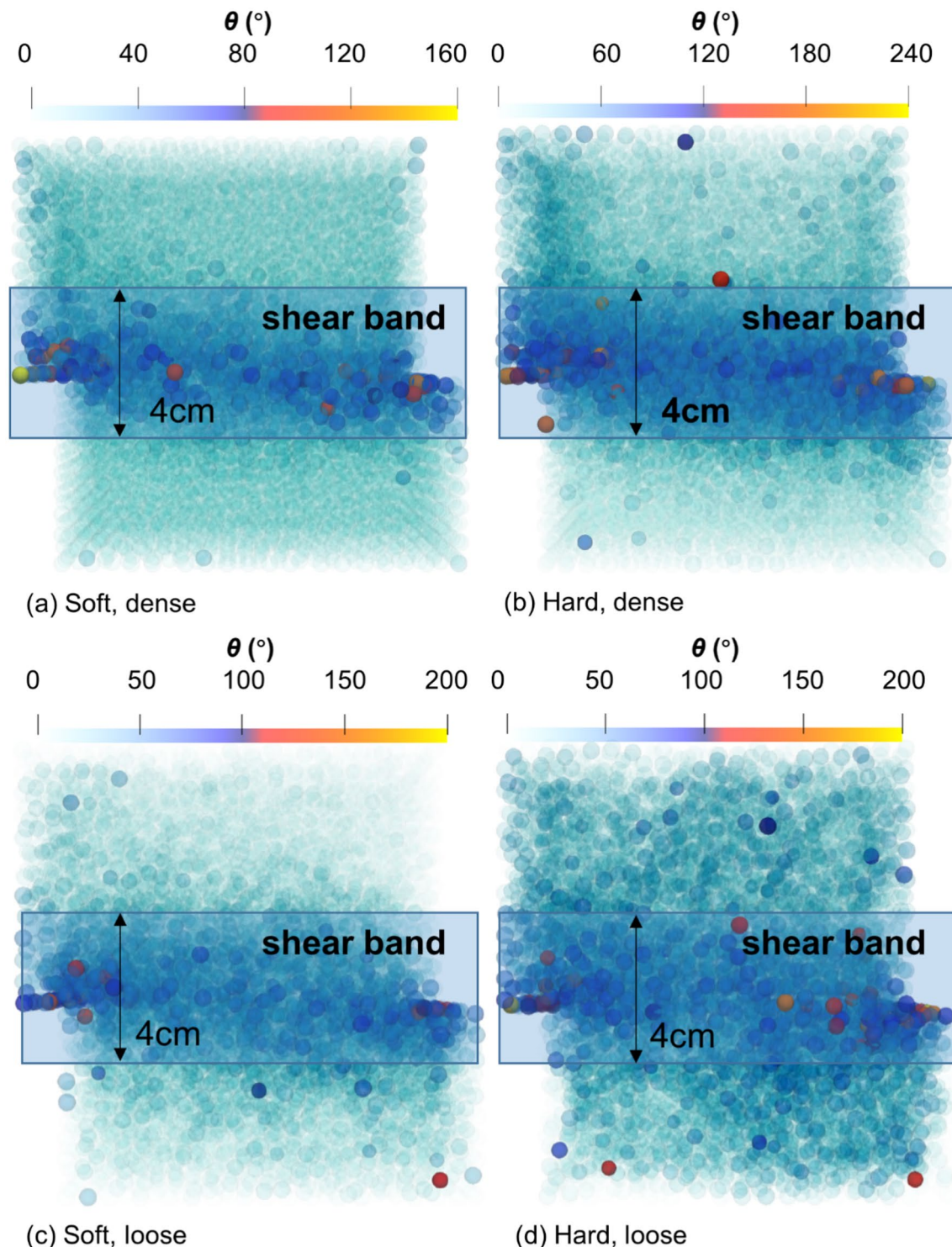


Fig. 13 Particle rotations using soft and hard contact models with $\mu=0.1$ at $\varepsilon_s=10\%$

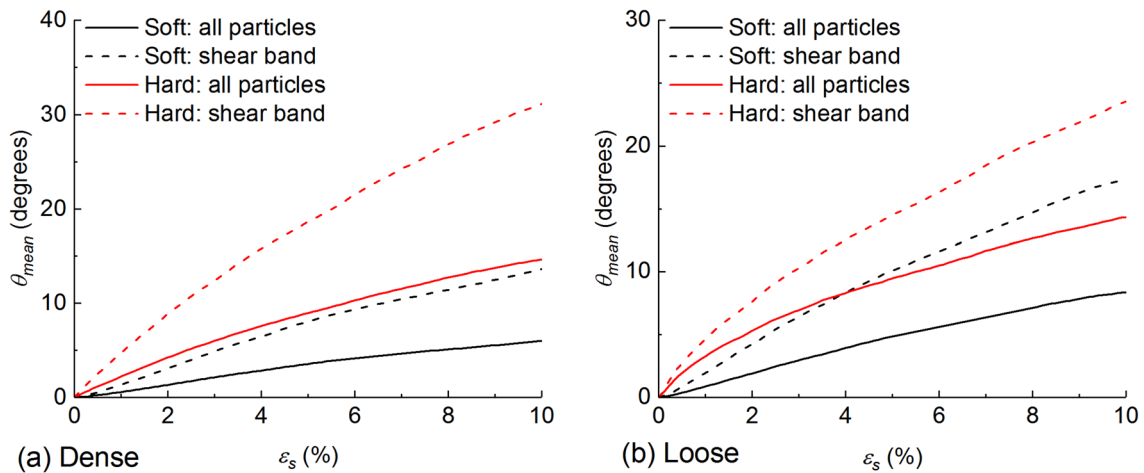


Fig. 14 Average particle rotations for all the particles and particles in shear bands using hard and soft contact models in **a** dense specimen and **b** loose specimen

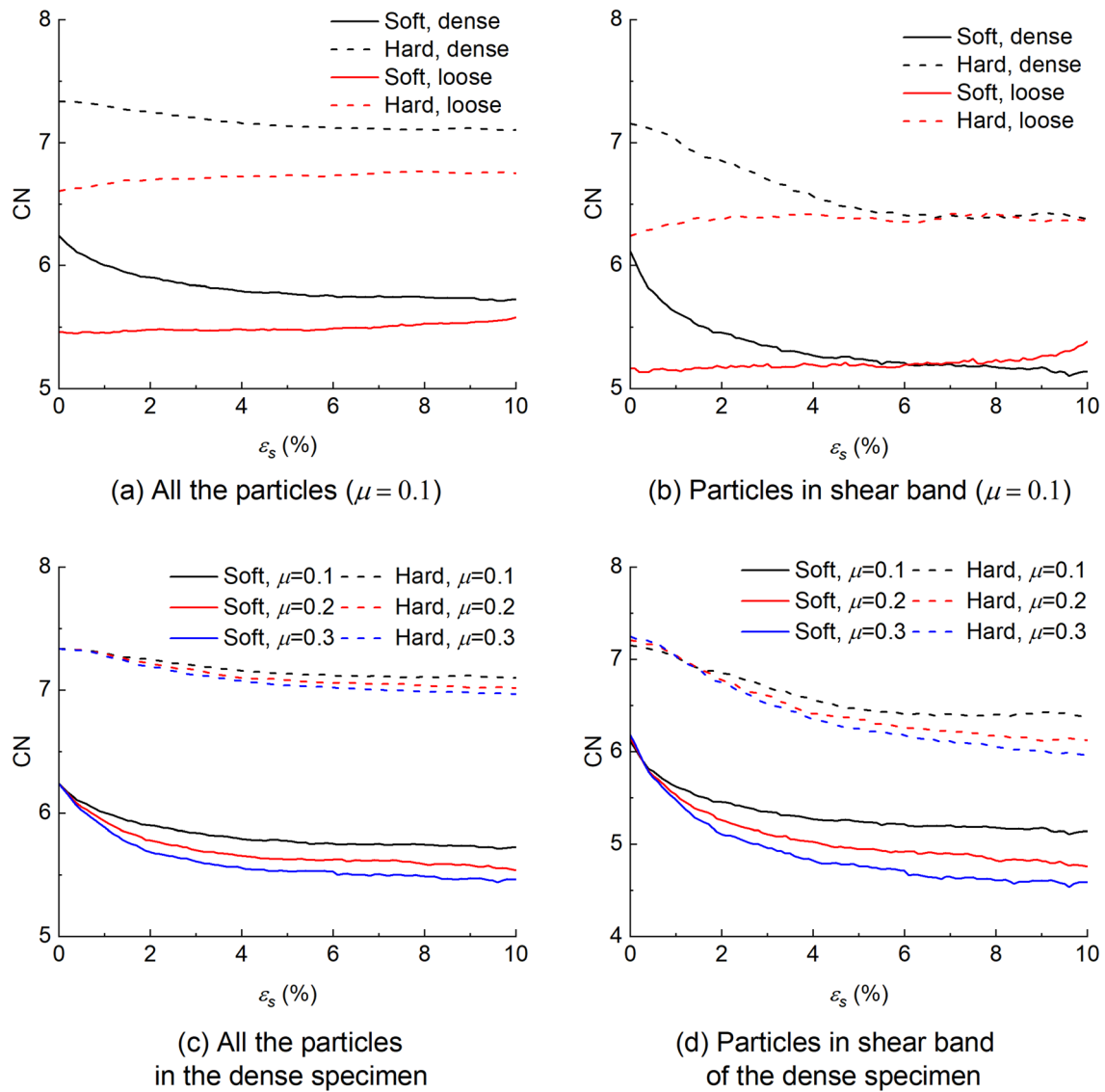
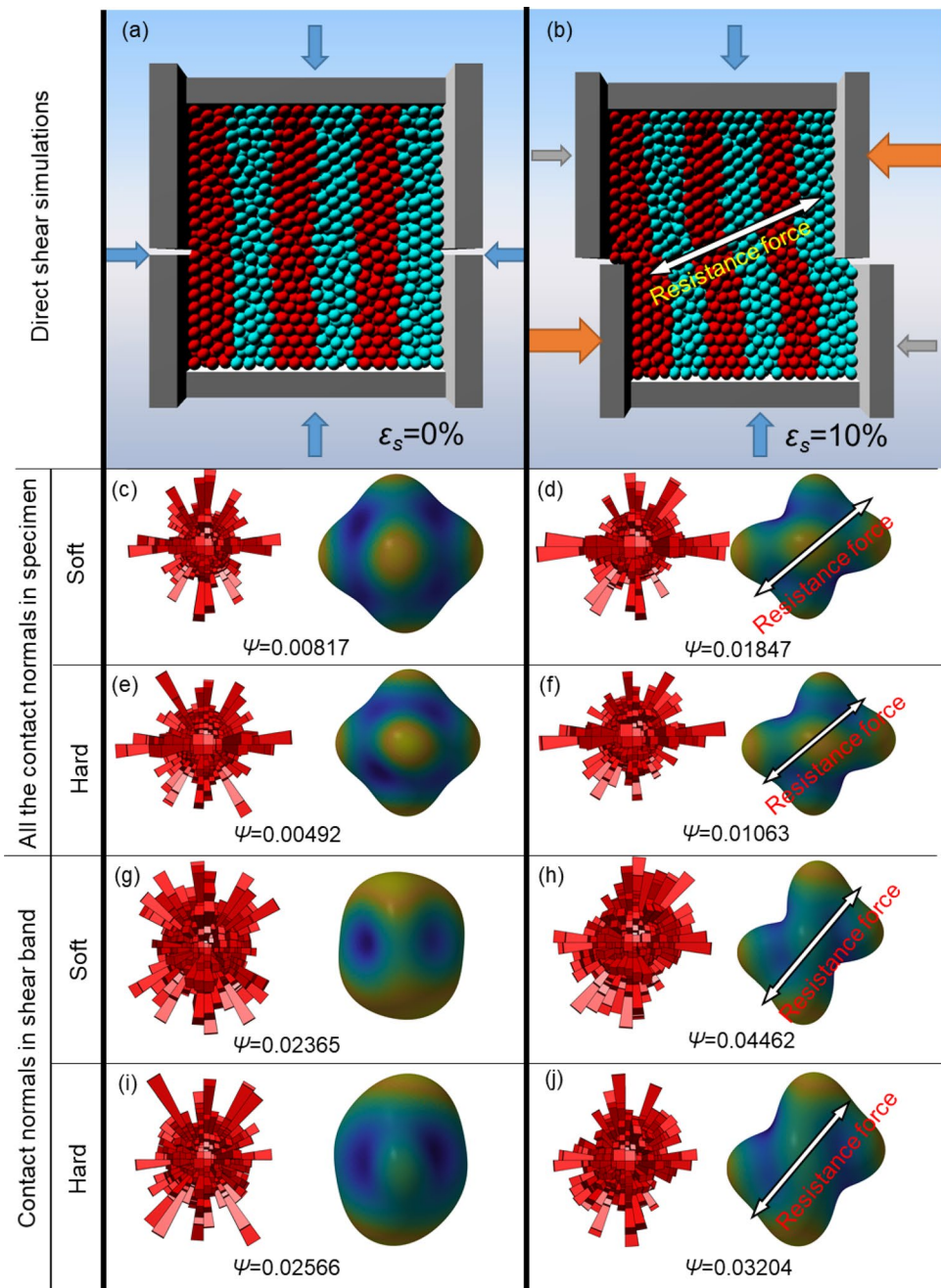


Fig. 15 The evolutions of coordination numbers

Fig. 16 Rose diagrams and density functions of contact normals before and after shear using hard and soft contact models with $\mu=0.1$



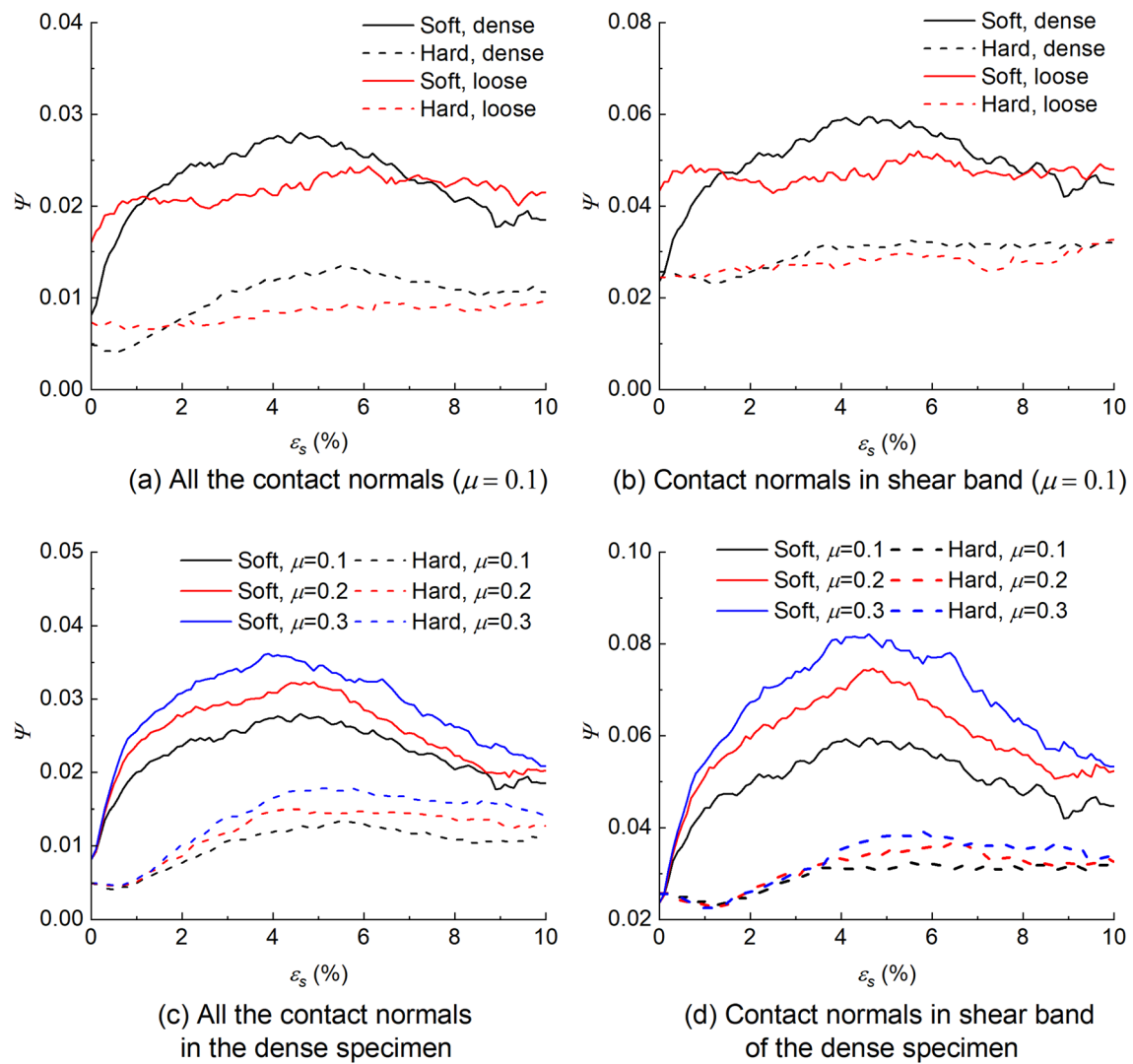


Fig. 17 The evolution of generalized octahedral fabric factors

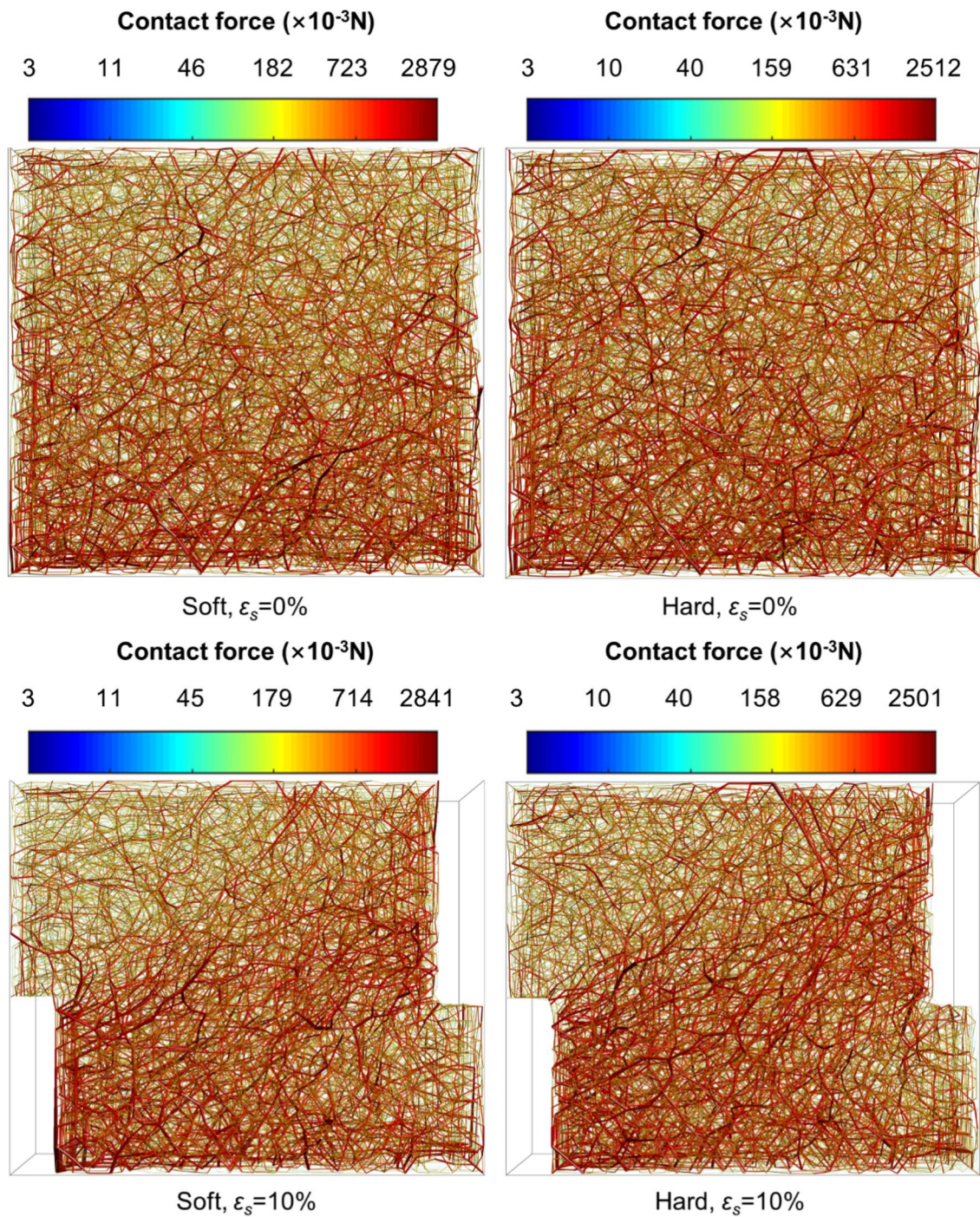


Fig. 18 Force chains before and after shear using hard and soft contact models with $\mu=0.1$

Acknowledgements This material is based upon work supported by the U.S. National Science Foundation under Grant No. CMMI 1917332. Any opinions, findings, and conclusions or recommendations expressed in this material are those of the authors and do not necessarily reflect the views of the National Science Foundation.

Compliance with ethical standards

Conflict of interest The authors declare that they have no conflict of interest.

References

1. Zheng J, Hryciw RD (2016) A corner preserving algorithm for realistic DEM soil particle generation. *Granul Matter* 18:84. <https://doi.org/10.1007/s10035-016-0679-0>
2. Zheng J, Hryciw RD (2017) An image based clump library for DEM simulations. *Granul Matter* 19:1–15. <https://doi.org/10.1007/s10035-017-0713-x>
3. Jing L, Kwok CY, Leung YF (2017) Micromechanical origin of particle size segregation. *Phys Rev Lett* 118:1–5. <https://doi.org/10.1103/PhysRevLett.118.118001>
4. Taghavi R (2011) Automatic clump generation based on mid-surface. In: Sainsbury B (ed) The 2nd international FLAC/DEM symposium. Itasca International Inc., Minneapolis, Melbourne, Bre-Anne Sainsbury pp 791–797
5. Kloss C, Goniva C, Hager A et al (2012) Models, algorithms and validation for opensource DEM and CFD-DEM. *Prog Comput Fluid Dyn Int J* 12:140–152. <https://doi.org/10.1504/PCFD.2012.047457>
6. Šmilauer V et al (2015) Yade documentation 2nd ed. The Yade Project. <https://doi.org/10.5281/zenodo.34073> (<http://yade-dem.org/doc/>)
7. Cundall PA (1971) A computer model for simulating progressive large scale movements in blocky rock systems. In: Symposium on international society on rock mechanics, vol 1, pp 129–136
8. Cundall PA, Strack ODL (1979) A discrete numerical model for granular assemblies. *Géotechnique* 29:47–65. <https://doi.org/10.1680/geot.1979.29.1.47>
9. Thornton C (1997) Coefficient of restitution for collinear collisions of elastic-perfectly plastic spheres. *J Appl Mech* 64:383. <https://doi.org/10.1115/1.2787319>
10. Galindo-Torres SA, Muñoz JD, Alonso-Marroquín F et al (2015) Frictional contact in collections of rigid or deformable bodies: numerical simulation of geomaterial motions. *Phys Rev E* 41:347–374. <https://doi.org/10.1103/physreve.70.061303>
11. Richefeu V, Radjai F, El Youssoufi MS et al (2006) Stress transmission in wet granular materials. *Eur Phys J E* 21:1–11. <https://doi.org/10.1140/epje/i2006-10077-1>
12. Lee SJ, Hashash YMA (2015) iDEM: an impulse-based discrete element method for fast granular dynamics. *Int J Numer Methods Eng* 104:79–103. <https://doi.org/10.1002/nme>
13. He H, Zheng J (2020) Simulations of realistic granular soils in oedometer tests using physics engine. *Int J Numer Anal Methods Geomech* 44:983–1002. <https://doi.org/10.1002/nag.3031>
14. Erez T, Tassa Y, Todorov E (2015) Simulation tools for model-based robotics: comparison of Bullet, Havok, MuJoCo, ODE and PhysX. In: Proceedings—IEEE international conference on robotics and automation, Seattle, pp 4397–4404
15. Klaus G, Glette K, Høvin M (2013) Evolving locomotion for a 12-DOF quadruped robot in simulated environments. *BioSystems* 112:102–106. <https://doi.org/10.1016/j.biosystems.2013.03.008>
16. Weiss T, Littenecker A, Jiang C, Terzopoulos D (2019) Position-based real-time simulation of large crowds. *Comput Graph* 78:12–22. <https://doi.org/10.1016/j.cag.2018.10.008>
17. Chui Y-P, Heng P-A (2010) Vaccination as a means of disease prevention. *Prog Biophys Mol Biol* 103:252–261. <https://doi.org/10.1016/j.pbiomolbio.2010.09.003>
18. Ermisoglu E, Sen F, Kockara S et al (2009) Scooping simulation framework for artificial cervical disc replacement surgery. In: Conference proceedings—IEEE international conference on systems, man and cybernetics
19. Craighead J, Murphy R, Burke J, Goldzie B (2007) A survey of commercial and open source unmanned vehicle simulators. In: Proceedings—IEEE international conference on robotics and automation
20. Xu J, Tang Z, Yuan X et al (2018) A VR-based the emergency rescue training system of railway accident. *Entertain Comput* 27:23–31. <https://doi.org/10.1016/j.entcom.2018.03.002>
21. Kim KJ, Cho SB (2015) Inference of other's internal neural models from active observation. *BioSystems* 128:37–47. <https://doi.org/10.1016/j.biosystems.2015.01.005>
22. Lim KW, Krabbenhoft K, Andrade JE (2014) A contact dynamics approach to the granular element method. *Comput Methods Appl Mech Eng* 268:557–573. <https://doi.org/10.1016/j.cma.2013.10.004>
23. Fleischmann J, Serban R, Negru D, Jayakumar P (2016) On the importance of displacement history in soft-body contact models. *J Comput Nonlinear Dyn* 11:1–5. <https://doi.org/10.1115/1.4031197>
24. Cundall PA (2001) A discontinuous future for numerical modelling in geomechanics? *Proc Inst Civ Eng Geotech Eng* 149:41–47. <https://doi.org/10.1680/geng.2001.149.1.41>
25. Tasora A, Serban R, Mazhar H et al (2016) Chrono: an open source multi-physics dynamics engine. In: Lecture notes in computer science (including subseries Lecture notes in artificial intelligence and lecture notes in bioinformatics)
26. Tasora A, Silvestri M, Righettini P (2007) Architecture of the Chrono:: engine physics simulation middleware. In: Proceedings of ECCOMAS 2007 multibody conference, pp 25–28
27. Datar M, Gorsich D, Lamb D, Negru D (2009) A framework for terrain-induced uncertainty quantification in vehicle dynamics simulation. *Int J Veh Syst Model Test* 4:234–255. <https://doi.org/10.1504/IJVSMT.2009.032018>
28. Recuero A, Serban R, Peterson B et al (2017) A high-fidelity approach for vehicle mobility simulation: nonlinear finite element tires operating on granular material. *J Terramech* 72:39–54. <https://doi.org/10.1016/j.jterra.2017.04.002>
29. Pazouki A, Kwarta M, Williams K et al (2017) Compliant contact versus rigid contact: a comparison in the context of granular dynamics. *Phys Rev E* 96:1–13. <https://doi.org/10.1103/PhysRevE.96.042905>
30. Tracy DJ, Buss SR, Woods BM (2009) Efficient large-scale sweep and prune methods with AABB insertion and removal. In: Proceedings of the IEEE virtual reality conference, pp 191–198
31. Horabik J, Molenda M (2016) Parameters and contact models for DEM simulations of agricultural granular materials: a review. *Biosyst Eng* 147:206–225. <https://doi.org/10.1016/j.biosystemseng.2016.02.017>
32. Tasora A, Anitescu M (2011) A matrix-free cone complementarity approach for solving large-scale, nonsmooth, rigid body dynamics. *Comput Methods Appl Mech Eng* 200:439–453. <https://doi.org/10.1016/j.cma.2010.06.030>
33. Cui L, O'Sullivan C (2006) Exploring the macro- and micro-scale response of an idealised granular material in the direct shear apparatus. *Géotechnique* 56:455–468. <https://doi.org/10.1680/geot.56.7.455>
34. O'Sullivan C, Bray JD, Riemer M (2004) Examination of the response of regularly packed specimens of spherical particles using physical tests and discrete element simulations. *J Eng Mech* 130:1140–1150. [https://doi.org/10.1061/\(ASCE\)0733-9399\(2004\)130:9\(1032\)](https://doi.org/10.1061/(ASCE)0733-9399(2004)130:9(1032))
35. ASTM D3080/D3080M-11 (2011) Standard test method for direct shear test of soils under consolidated drained conditions. ASTM International, West Conshohocken
36. Fonseca J, O'Sullivan C, Coop MRR, Lee PDD (2013) Quantifying the evolution of soil fabric during shearing using directional parameters. *Géotechnique* 63:487–499. <https://doi.org/10.1680/geot.12.P.003>

37. Fonseca J, O'Sullivan C, Coop MR, Lee PD (2013) Quantifying the evolution of soil fabric during shearing using scalar parameters. *Géotechnique* 63:818–829. <https://doi.org/10.1680/geot.11.P.150>
38. Kanatani K (1984) Distribution of directional data and fabric tensors. *Int J Eng Sci* 22:149–164
39. Dafalias YF, Papadimitriou AG, Li XS (2004) Sand plasticity model accounting for inherent fabric anisotropy. *J Eng Mech* 130:1319–1333. [https://doi.org/10.1061/\(ASCE\)0733-9399\(2004\)130:11\(1319\)](https://doi.org/10.1061/(ASCE)0733-9399(2004)130:11(1319))
40. Dafalias YF, Li XS, Dafalias YF (2004) A constitutive framework for anisotropic sand including non-proportional loading. *Géotechnique* 54:41–55. <https://doi.org/10.1680/geot.54.1.41.36329>
41. Gao Z, Zhao J, Yao Y (2010) A generalized anisotropic failure criterion for geomaterials. *Int J Solids Struct* 47:3166–3185. <https://doi.org/10.1016/j.ijsolstr.2010.07.016>
42. Gao Z, Zhao J (2013) Strain localization and fabric evolution in sand. *Int J Solids Struct* 50:3634–3648. <https://doi.org/10.1016/j.ijsolstr.2013.07.005>
43. Zhao J, Gao Z (2016) Unified anisotropic elastoplastic model for sand. *J Eng Mech* 142:04015056. [https://doi.org/10.1061/\(ASCE\)EM.1943-7889.0000962](https://doi.org/10.1061/(ASCE)EM.1943-7889.0000962)
44. Barreto D, O'Sullivan C (2012) The influence of inter-particle friction and the intermediate stress ratio on soil response under generalised stress conditions. *Granul Matter* 14:505–521. <https://doi.org/10.1007/s10035-012-0354-z>

Publisher's Note Springer Nature remains neutral with regard to jurisdictional claims in published maps and institutional affiliations.